Optimal Design of Soft Pneumatic Bending Actuators Subjected to Design-Dependent Pressure Loads

Yongyu Chen, Zeyang Xia, *Senior Member, IEEE*, and Qunfei Zhao

***Abstract*—Soft actuators, mainly composed of soft materials, have made a great impact on applications in unstructured or unknown environments due to their high flexibility and customizability. The design methods of soft actuators can be divided into two groups: the bionic design method and the topology optimization method. Compared to the bionic design method that requires numerous experiments, the topology optimization method can generate innovative structures according to the design requirements. However, the existing topology optimization method cannot be applied to soft pneumatic bending actuator (SPBA) designs because SPBAs are usually subjected to design-dependent pressure loads of which the position depends on the structure. In this paper, we propose an optimal design framework of SPBAs to resolve the design-dependent load problem using an adaptive bi-directional evolutionary structural optimization method. Herein, SPBAs are considered as compliant mechanisms and our goal is to achieve maximum bending deformation as well as structural stiffness. In finite element analysis, each element in the design domain is set to solid or void according to sensitivity number, which is approximated by the objective function derivative with respect to the design variables. During the iterative optimization procedure, we explicitly define the movable solid-void boundary surfaces on which the pressure will act. A precision prototype actuator is fabricated, and its performance is evaluated in terms of free travel experiment. Some extensions are supplied to validate the optimality and reliability of the proposed method. This framework paves a way for the diversity of soft actuators.**

***Index Terms*—Design-dependent pressure loads, finite element analysis (FEA), soft pneumatic bending actuators (SPBAs), topology optimization.**

Manuscript received July 19, 2019; accepted September 16, 2019. Date of publication September 24, 2019; date of current version December 31, 2019. Recommended by Technical Editor H. R. Choi. This work was supported in part by the National Key Project of Research and Development Plan of China Inter-Governmental Cooperative Science and Technology Project (2016YFE0128000), in part by the National Science Foundation of China (61773365 and 61811540033), and in part by the Fundamental Research Program of Shenzhen (JCYJ20170413162458312). *(Corresponding author: Zeyang Xia.)*

Y. Chen and Q. Zhao are with the Department of Automation, Shanghai Jiao Tong University, Shanghai 200240, China (e-mail: idiot--xiaotou@sjtu.edu.cn; zhaoqf@sjtu.edu.cn).

Z. Xia is with the CAS Key Laboratory of Human-Machine Intelligence-Synergy Systems, Shenzhen Institutes of Advanced Technology, Chinese Academy of Sciences, Shenzhen 518055, China (e-mail: zy.xia@siat.ac.cn).

Color versions of one or more of the figures in this article are available online at http://ieeexplore.ieee.org.

Digital Object Identifier 10.1109/TMECH.2019.2943418

I. Introduction

SOFT robotics has become a hot research area that utilizes the flexibility and adaptability of soft materials to unlock robotic motion for soft interaction with the environment. The development of soft robots made up of soft materials like elastomers are highly promoted by many applications ranging from medical to industrial usages [1]. Soft robots have the potential to deform their bodies in multiple degrees of freedom and thus can be used in confined spaces [2]; to support activities of daily living for hand assistance and rehabilitation [3]; to pick and place variable shapeless objects as soft grippers [4]; to search for natural disaster relief as industrial robots [5]; or to be embedded in artificial muscles for human–robot interactions [6]. The key fundamental part of the soft robotic system is the soft actuator. The soft actuator is a chief component responsible for moving or controlling the soft robotic system. The diversity of applications in soft robots leads us to the following research question: How do we design the structure of soft actuators conditioned on customized requirements? From a structural perspective, the design methods of soft actuators can be divided into two groups: the bionic design method and the topology optimization method.

The bionic design method enables the soft actuators to mimic the dexterous locomotion of fishes [7], worms [8], octopus [9], and human fingers [10]. To implement the functional diversities, most soft-actuator prototypes use pneumatic actuation and aim at achieving bending motion. They are known as soft pneumatic bending actuators (SPBAs). From the bionic designs, SPBAs can be reduced to two basic structures including pneumatic networks (PneuNets) [11] and fiber-reinforced structures [12]. Although these two basic structures are effectual, novel SPBAs based on them are primarily dependent on researchers' intuition and experience. To design SPBAs that can meet customized requirements, researchers make a guess on the initial structure and improve them through experiments. In other words, the soft actuator designs using bionic methods have to undergo a hypothesis-to-test process, which is time consuming, costly, and limited in creating novel soft actuators.

Contrarily, the topology optimization method does not rely on the initial structure and researchers' experience so that the soft actuator designs using topology optimization method may obtain innovative structures. In order to model and design the soft actuators automatically, researchers found that the soft actuator design problem can be regarded as the topology optimization

problem of continuum compliant mechanisms [13]. So far some efforts have been made toward the topology optimization methods of soft actuators. Hiller *et al*. [14] adopted the genetic algorithm to design freeform soft robots for the forward locomotion. But this kind of robots had to work in a closed vacuum atmosphere. Zhang *et al*. [15] designed the soft fingers using the solid isotropic material with penalization (SIMP) method. These soft fingers had one actuation tube in the center and changed the topology outside the tube. However, they showed poor performance on bending ability. Chen *et al*. [16] utilized the level set method to develop a soft gripper driven by cables. All of these methods were applied to the soft actuators subjected to fixed loads. It means that they cannot be applied on SPBAs subjected to pressure loads of which the position depends on the structure. This kind of load is called design-dependent [17] load. Therefore, the design of SPBAs is in need of a topology optimization method to automatically create novel SPBAs.

In this paper, we propose a design framework for SPBA designs conditioned on customized requirements using topology optimization method. During the topology optimization process, internal cavities may be introduced automatically in order to achieve the optimal structure. In each iteration, the generated cavities lead to the solid-void boundary surfaces on which the pressure will act. Specifically, to resolve the design-dependent pressure load problem, we present an adaptive bi-directional evolutionary structural optimization (BESO) method [18]. Compared to other topology optimization methods including the SIMP method and the level set method, the BESO method is capable of removing the soft elements completely and can be easily integrated with advanced finite element analysis (FEA) [19]. After recasting SPBAs as compliant mechanisms, the design goal is to mathematically seek the optimal topologies so that the mechanical flexibility can reach a maximum level. Considering the reusability and extensibility, the proposed BESO method is abstract in mathematics. This means that we generalize the method as much as possible to satisfy various specific requirements for SPBA designs.

Within our well-structured optimal design framework, the BESO method is easily implemented using FEA software. The final optimized results are simulated under nonlinear FEA and validated through experiments to characterize the mechanical behavior. To shed light on the extensibility of the proposed method, we present several examples of modifications to the customized requirements, by adding an unstretchable layer in the bottom, starting from an initial guess design, changing the geometric shape, and replacing the optimization objective. As a result, a variety of novel SPBAs are created and all of them show great performance on bending ability.

II. Methodology

A. Design Requirement

The optimal design problem of an SPBA concerns the design requirement of maximizing its bending deformation according to geometry, material property, boundary conditions, and load cases. As the structure domain is discretized into a fine mesh of elements on the basis of FEA, the objective is to find the optimal structures by determining for every element in the design domain whether there should be material (solid element) or not (void element). Herein, the void regions are considered to be chambers. The pneumatic pressure is modeled simply as design-dependent pressure loads on the face of each internal surface.

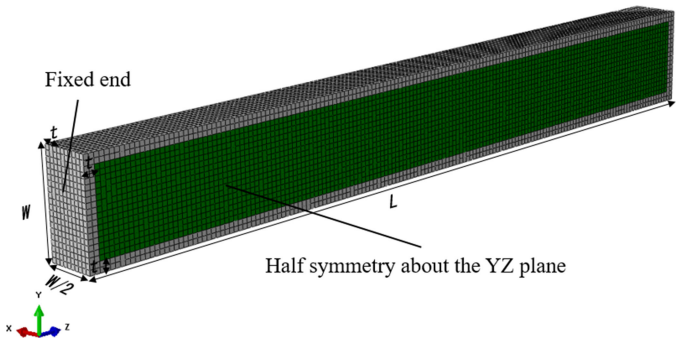

Fig. 1. Prototype of an SPBA indicating the dimensional parameters and boundary conditions. The SPBA is modeled in half-symmetry. Note that the design domain is in green color while the off-design domain is in white color.

To start with an example, the SPBA is initialized as a rectangular solid of length L, and width and height W. The design domain is embedded into the actuator and the wall thickness is set to the value of t (see Fig. 1). In this paper, twisting effect of SPBAs is ignored because we only care about the bending ability. Therefore, the structure is symmetric and only half the portion of the entire actuator is created and modeled for the sake of simplifying the computational complexity. The geometric parameters of the actuator can be customized according to the specific design requirements. The boundary conditions include half-symmetry, as mentioned previously, and no translation or rotation for one end of the actuator. As for the input loads, the surface that the pressure loads will act upon needs to be defined before running FEA. This surface is made up of all the faces of the inner cavity of the actuator, which is obtained by identifying the solid-void boundary.

B. Problem Formulation

The SPBA design problem is formulated as the topology optimization of compliant mechanisms with design-dependent loads. In the case of topology optimization of common compliant mechanisms, the previous works used the output displacement u_{out} as the objective function most often. As for the SPBA designs, u_{out} can be evaluated by calculating the downward displacement at the tip of an SPBA (see Fig. 2). However, this single choice may result in disconnected topologies and convergence problems [20].

Actually, the objective function for SPBA designs must consider not only the mechanical flexibility but also the structural stiffness to apply external loads. Although the required flexibility and stiffness are contrary design objectives, a compromise between both characteristics can be established to correctly address the problem using a multi-criteria optimization strategy [20]. The maximum flexibility can be accomplished by maximizing

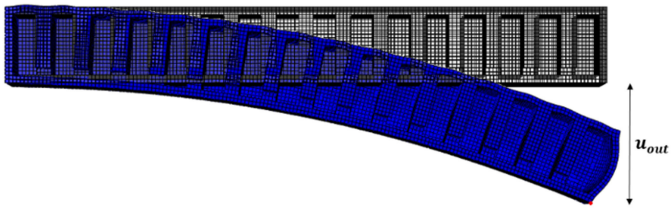

Fig. 2. FEA simulation revealing the calculation of u_{out}.

the displacement, while the maximum stiffness is equivalent to minimizing the compliance or the external work done by the pressure loads. Maximizing the structural stiffness also has the advantage that SPBAs can undergo higher pressure and thus generate higher resultant force, which helps them actuate more effectively and efficiently. Since the displacement needs to be maximized and the compliance minimized, the easy way to combine them is the use of a ratio. In addition, the downward displacement u_{out} is a negative value going along the negative y-axis under such coordinate system shown in Fig. 1.

The examples considered in this paper are aimed at satisfying the two objectives discussed above with volume constraints of the structure under design-dependent pressure loads. In the BESO method, a structure is optimized by removing or adding elements, that is, the element itself is treated as the design variable instead of its associated physical or material parameters. Therefore, the evolutionary topology optimization problem of SPBA can be formulated as

$$\begin{aligned} &\text{Minimize}: \ h\left(x_1,\ x_2,\ \ldots,\ x_N\right) = \tfrac{u_{\text{out}}}{C} \\ &\text{With}: \quad u_{\text{out}} = \boldsymbol{L_{\text{out}}}^{\boldsymbol{T}}\boldsymbol{U} \\ &\qquad\quad C = \tfrac{1}{2}\boldsymbol{F^T U} \\ &\text{Subject to}: V^* - \sum_{e=1}^{N} V_e x_e = 0 \\ &\qquad\quad x_e = 0 \text{ or } 1 \end{aligned} \tag{1}$$

where N is the total number of discretized elements in the design domain. The binary design variable x_e indicates that the *eth* element is void ($x_e = 0$) or solid ($x_e = 1$). $\boldsymbol{L_{\text{out}}}$ is a one-hot vector full of 0s except for a 1 at the output node corresponding to the downward displacement. $\boldsymbol{F}$ and $\boldsymbol{U}$ are the applied load and displacement vectors. V_e and V^* represent the volume of an individual element and the prescribed total structural volume, respectively.

C. Sensitivity Analysis and Sensitivity Number

In the BESO method, the element sensitivity denotes the objective function gradient. To minimize the objective function through the removal of elements, it is evident that the most effective way is to eliminate the elements that have the lowest values of the sensitivity so that the increase in $h(x_1,\ x_2,\ \ldots,\ x_N)$ will be minimal [18]. Assuming that the design variable changes continuously from 1 to 0, the derivative of $h(x_1,\ x_2,\ \ldots,\ x_N)$ can be determined by

$$\frac{\partial h}{\partial x_e} = \frac{\frac{\partial u_{\text{out}}}{\partial x_e} C - \frac{\partial C}{\partial x_e} u_{\text{out}}}{C^2}. \tag{2}$$

The following step is to find two expressions for the sensitivity of the mechanical flexibility and the structural stiffness, i.e., $\partial u_{\text{out}}/\partial x_e$ and $\partial C/\partial x_e$, which are derived as

$$\frac{\partial u_{\text{out}}}{\partial x_e} = \frac{\partial(\boldsymbol{L_{\text{out}}}^T \boldsymbol{U})}{\partial x_e} = \boldsymbol{L_{\text{out}}}^T \frac{\partial \boldsymbol{U}}{\partial x_e} \tag{3}$$

$$\frac{\partial C}{\partial x_e} = \frac{\partial\left(\frac{1}{2}\boldsymbol{F}^T\boldsymbol{U}\right)}{\partial x_e} = \frac{1}{2}\frac{\partial\left(\boldsymbol{F^T}\right)}{\partial x_e}\boldsymbol{U} + \frac{1}{2}\boldsymbol{F^T}\frac{\partial \boldsymbol{U}}{\partial x_e}. \tag{4}$$

In FEA, the static equilibrium equation of a structure is expressed as

$$\begin{aligned} \boldsymbol{KU} &= \boldsymbol{F} \\ \boldsymbol{U^T K} &= \boldsymbol{F^T} \end{aligned} \tag{5}$$

where the global stiffness matrix $\boldsymbol{K}$ is symmetric and positive semidefinite.

Deriving it and reorganizing the terms, the displacement sensitivity multiplied by the global stiffness matrix can be found as follows:

$$\begin{aligned} \frac{\partial\left(\boldsymbol{KU}\right)}{\partial x_e} &= \frac{\partial \boldsymbol{F}}{\partial x_e} \\ \boldsymbol{K}\frac{\partial \boldsymbol{U}}{\partial x_e} &= -\frac{\partial \boldsymbol{K}}{\partial x_e}\boldsymbol{U} + \frac{\partial \boldsymbol{F}}{\partial x_e}. \end{aligned} \tag{6}$$

With (6) we can rewrite the expressions for $\partial u_{\text{out}}/\partial x_e$ and $\partial C/\partial x_e$ using (3) and (4) as

$$\frac{\partial u_{\text{out}}}{\partial x_e} = (\boldsymbol{K\lambda})^{\boldsymbol{T}}\frac{\partial \boldsymbol{U}}{\partial x_e} = \boldsymbol{\lambda^T}\left(-\frac{\partial \boldsymbol{K}}{\partial x_e}\boldsymbol{U} + \frac{\partial \boldsymbol{F}}{\partial x_e}\right) \tag{7}$$

$$\begin{aligned} \frac{\partial C}{\partial x_e} &= \frac{1}{2}\frac{\partial\left(\boldsymbol{F^T}\right)}{\partial x_e}\boldsymbol{U} + \frac{1}{2}\boldsymbol{U^T}\left(-\frac{\partial \boldsymbol{K}}{\partial x_e}\boldsymbol{U} + \frac{\partial \boldsymbol{F}}{\partial x_e}\right) \\ &= \frac{\partial\left(\boldsymbol{F^T}\right)}{\partial x_e}\boldsymbol{U} - \frac{1}{2}\boldsymbol{U^T}\frac{\partial \boldsymbol{K}}{\partial x_e}\boldsymbol{U} \end{aligned} \tag{8}$$

where the vector $\boldsymbol{\lambda}$ represents the displacement response to the virtual load vector $\boldsymbol{L_{\text{out}}}$. In fact, the adjoint method is used to determine the virtual displacement vector due to the equilibrium equation as

$$\boldsymbol{K\lambda} = \boldsymbol{L_{\text{out}}}. \tag{9}$$

The global stiffness matrix $\boldsymbol{K}$ can be expressed by the design variables x_e. Material interpolation schemes with penalization is utilized for achieving a solid-void design, which is very similar to the SIMP method. As the sensitivity of the objective function can be both positive and negative, the nonmonotonous behavior may be generated [21]. Due to this reason, we consider a special interpolation scheme instead of the power law material model, which is known as the rational approximation of material properties [22]. It has been shown to simply handle the design-dependent loading problems. Young's modulus of the intermediate material model is given as

$$E\left(x_e\right) = \frac{x_e}{1 + q\left(1 - x_e\right)}E_0 \tag{10}$$

where E_0 denotes Young's modulus of the solid material and q the penalty factor that is larger than 0 for topology optimization problems. It is assumed that the Poisson's ratio is independent

of the design variables and thus the matrix $\boldsymbol{K}$ is

$$\boldsymbol{K} = \sum_{e=1}^{N} E(x_e)\,\boldsymbol{K_e} \tag{11}$$

where $\boldsymbol{K_e}$ is a global version of the element stiffness matrix $\boldsymbol{K_e^0}$. The elements of $\boldsymbol{K_e}$ are all zeroes except those that correspond to the degrees of freedom of the mesh nodes associated with the *eth* element. Note that the dimension of $\boldsymbol{K_e^0}$ is 24×24 because each brick element is associated with eight nodes and each node has three degrees of freedom.

In order to allow the complete removal of void elements from the design domain, the BESO method is developed using a hard-kill technique, where the densities of the void elements are set to zero. Moreover, totally removing the soft elements is devised to circumvent the problems that the element stiffness matrix may change caused by large deformation of SPBAs [23]. Thus, the derivative of the global stiffness matrix is expressed as

$$\begin{aligned}\frac{\partial \boldsymbol{K}}{\partial x_e} &= \frac{1+q}{[1+q(1-x_e)]^2}\boldsymbol{K_e} \\ &= \begin{cases} (1+q)\,\boldsymbol{K_e}, & |x_e = 1 \\ \dfrac{1}{1+q}\boldsymbol{K_e}, & |x_e = 0 \end{cases}.\end{aligned} \tag{12}$$

The derivative of the actuation force $\partial \boldsymbol{F}/\partial x_e$ also needs to be evaluated. Using an approximation based on the FEA, the force acting on the SPBA provided by the pneumatic pressure is

$$\boldsymbol{F} = p_0 \boldsymbol{L_p} \tag{13}$$

where the constant p_0 denotes the actuation force acting on a unit area. $\boldsymbol{L_p}$ indicates the normal direction of the solid-void boundary.

The derivative of the matrix $\boldsymbol{L_p}$ indicates the change in the loading condition due to the *eth* element removal. No matter what the initial structure, the change $\partial \boldsymbol{L_p}/\partial x_e$ for a brick element always ends up in a single form similar to the ones that can be found in the literature [24], [25]. It represents the change in pressure loads when a solid element is removed and a void element full with air replaces it. From Fig. 2, we can assume that removing an element transfers the intra-surface pressure through six sides of the whole brick element.

Therefore, taking an eight-node linear brick element, for example, the load change in the *eth* element can be evaluated considering the normal vector $\boldsymbol{L_p}$ outward from the void element. In the coordinate system shown in Fig. 2, it can be directly expressed as

$$\begin{aligned}\Delta \boldsymbol{l_p} = \frac{1}{4}S[&-1,1,1,\ -1,-1,1,\ -1,-1,-1,\ -1,1,\\ &-1,\ 1,1,1,\ 1,-1,1,\ 1,-1,-1,1,1,-1]^T\end{aligned} \tag{14}$$

where S is the area of the element's each surface. It is noted that $\Delta \boldsymbol{l_p}$ is to $\partial \boldsymbol{L_p}/\partial x_e$ what $\boldsymbol{K_e^0}$ is to $\boldsymbol{K_e}$. $\partial \boldsymbol{L_p}/\partial x_e$ is a sparse vector whose nonzero elements are the elements of $\Delta \boldsymbol{l_p}$.

By substituting the above-mentioned equation into (2) and ignoring the redundant zero values of the matrices and vectors, the sensitivity of the objective function with regard to the change in the *eth* element can be found as

$$\begin{aligned}\frac{\partial h}{\partial x_e} = \frac{1}{C^2}\Bigg[C\Bigg(&-\frac{1+q}{[1+q(1-x_e)]^2}\boldsymbol{\lambda_e^T K_e^0 u_e} \\ &+ p_0 \boldsymbol{\lambda_e^T}\Delta \boldsymbol{l_p}\Bigg) - u_{\text{out}}\Bigg(-\frac{1}{2}\frac{1+q}{[1+q(1-x_e)]^2}\boldsymbol{u_e^T} \\ &\boldsymbol{K_e^0 u_e} + p_0 \Delta \boldsymbol{l_p}^T \boldsymbol{u_e}\Bigg)\Bigg]\end{aligned} \tag{15}$$

where $\boldsymbol{\lambda_e}$ is the virtual displacement vector of the *eth* element and $\boldsymbol{u_e}$ is the displacement vector of the *eth* element.

In such a case, SPBA is optimized using fully discrete design variables. Accordingly, the element sensitivity number can be defined by the relative ranking of the sensitivity of an individual element as

$$\begin{aligned}\alpha_e &= -\frac{C^2}{1+q}\frac{\partial h}{\partial x_e} \\ &= \begin{cases} C\left(\boldsymbol{\lambda_e^T K_e^0 u_e} - \dfrac{1}{1+q}p_0 \boldsymbol{\lambda_e^T}\Delta \boldsymbol{l_p}\right) \\ -u_{\text{out}}\left(\dfrac{1}{2}\boldsymbol{u_e^T K_e^0 u_e} - \dfrac{1}{1+q}p_0 \Delta \boldsymbol{l_p}^T \boldsymbol{u_e}\right)(x_e = 1) \\ C\left(\dfrac{1}{(1+q)^2}\boldsymbol{\lambda_e^T K_e^0 u_e} - \dfrac{1}{1+q}p_0 \boldsymbol{\lambda_e^T}\Delta \boldsymbol{l_p}\right) \\ -u_{\text{out}}\left(\dfrac{1}{2(1+q)^2}\boldsymbol{u_e^T K_e^0 u_e} - \dfrac{1}{1+q}p_0 \Delta \boldsymbol{l_p}^T \boldsymbol{u_e}\right)(x_e = 0) \end{cases}.\end{aligned} \tag{16}$$

It is seen that the sensitivity numbers depend on the selection of the penalty factor q. When q tends to infinity, the above-mentioned sensitivity number reduces to the following simple expressions:

$$\alpha_e = \begin{cases} C\boldsymbol{\lambda_e^T K_e^0 u_e} - \dfrac{1}{2}u_{\text{out}}\boldsymbol{u_e^T K_e^0 u_e}\ (x_e = 1) \\ 0 \qquad\qquad\qquad\qquad\qquad\quad (x_e = 0) \end{cases}. \tag{17}$$

Actually, the selection of the penalty factor does affect the relative ranking of the sensitivity numbers and may result in a different solution. Nevertheless, it is still worth using an infinite penalty factor. On the one hand, high computational efficiency is obtained. On the other hand, noting that u_{out} is negative we find that the nonmonotonous behavior disappears completely as is evident from (17).

D. Filtering Scheme and Improved Sensitivity Number

The raw sensitivity usually causes checkerboard patterns and mesh-dependency problems [18]. To overcome these problems, the sensitivity filtering scheme will be introduced into the BESO method. This simple filtering scheme can be visualized by drawing a sphere of radius $r_{\min}$ centered at the centroid of the *eth* element, thus generating the globose subdomain Ω_e. Usually the value of $r_{\min}$ should be big enough so that Ω_e covers more than one element. As a result, the improved sensitivity number

of the *eth* element becomes

$$\alpha_e = \frac{\sum_{i=1}^{M} w(r_{ei})\,\alpha_i}{\sum_{i=1}^{M} w(r_{ei})} \quad \text{With}: \quad w(r_{ei}) = r_{\min} - r_{ei}\ (i = 1,\ 2,\ \ldots,\ M) \tag{18}$$

where *M* denotes the total number of elements in the subdomain Ω_e and r_{ei} is the distance between the center of elements *e* and *i*.

The filtering scheme smooths the sensitivity numbers in the whole design domain. Additionally, the sensitivity numbers of void elements may not be zero due to nonzero sensitivity numbers of solid elements within the subdomain. This means that some of the void elements may be changed to solid elements in the next iteration.

The linear weight factor $w(r_{ei})$ of each element must be calculated before the main BESO method starts because it takes a long time to be accomplished. Thankfully, if the initial structure is not changed, the calculated value of $w(r_{ei})$ can be used in each simulation.

Finally, to stabilize the evolutionary process and make the topology easy to converge, the sensitivity number is averaged with its historical information [18] as

$$\alpha_e = \frac{\alpha_e^k + \alpha_e^{k-1}}{2} \tag{19}$$

where *k* is the current iteration number. Then update the sensitivity number and let $\alpha_e^k = \alpha_e$, which will be used for the next iteration.

E. Element Removal/Addition and Convergence Criterion

Before elements are removed from or added to the current design, the target volume for the next iteration V_{k+1} needs to be given first. Since the volume constraint V^* can be greater or smaller than the volume of the current iteration, the target volume of the next iteration may either decrease or increase. The evolution of the volume can be expressed by

$$V_{k+1} = \begin{cases} V_k\,(1+ER) & (V_k < V^*) \\ V_k\,(1-ER) & (V_k > V^*) \\ V^* & (V_k = V^*) \end{cases} \tag{20}$$

where ER is the evolutionary volume ratio.

Then all the elements, both solid and void, are sorted in descending order according to the values of their sensitivity numbers. For solid elements $(x_e = 1)$, it will be removed (x_e is switched to 0) if

$$\alpha_e \le \alpha_{th}. \tag{21}$$

For void element $(x_e = 0)$, it will be added (x_e is switched to 1) if

$$\alpha_e \ge \alpha_{th} \tag{22}$$

where α_{th} is the threshold sensitivity numbers for removing and adding elements. Here α_{th} is used to satisfy the volume of next iteration V_{k+1}. For example, there are 10 000 ordered elements in the design domain and $\alpha_1 \ge \alpha_2 \ge \cdots \ge \alpha_{10000}$ and if V_{k+1} equals to 90%, then $\alpha_{th} = \alpha_{9000}$.

However, there may be too many elements added into the structure during a single iteration. It could make the structure lose its integrity and stability. Therefore, the volume addition ratio (AR) is introduced to solve this problem [18]. AR is defined as the number of added elements divided by the total number of elements in the design domain. The parameter $AR_{\max}$ is introduced and once $AR > AR_{\max}$, only some of the elements with higher sensitivity numbers are added so as to satisfy $AR = AR_{\max}$.

Finally, the cycle of FEA and element removal/addition continues until the constrained volume V^* is reached and the following convergence criterion is satisfied:

$$\text{error} = \left| \frac{\sum_{i=1}^{S} h_{k-i+1} - \sum_{i=1}^{S} h_{k-S-i+1}}{\sum_{i=1}^{S} h_{k-i+1}} \right| \le \tau \tag{23}$$

where τ is the allowable convergence tolerance and *S* is an integer number. In this case, *S* is selected to be 5, which implies that the change in the objective function over the last ten iterations is acceptably small.

III. Numerical Implementation and Results

A. Numerical Implementation and Evolutionary Procedure

The BESO method is programmed in Python and integrated with the commercial software ABAQUS that is used as FEA solver. General static numerical solutions are obtained to model the response of SPBAs. To make the evolutionary iteration fully automatic, ABAQUS scripting is utilized, which saves much time and effort. The evolutionary iteration procedure of the present BESO method for SPBA designs is given as follows.

1) Initialize the structure from the full design in ABAQUS, including discretizing the structure using a finite element mesh, assigning material properties, and defining the boundary and loading conditions.
2) Perform FEA for the structure to obtain the ABAQUS output database and then calculate the element sensitivity number according to (17).
3) Apply the filtering scheme on the element sensitivity numbers using (18), compute average from the previous results using (19), and then save the results for next iteration.
4) Determine the target volume for the next iteration using (20) and then add or delete elements according to the procedure described in Section II-E.
5) Reconstruct a new SPBA design in ABAQUS by switching design variables x_e. It should be pointed out that the loading conditions also need to be changed because of the movable solid-void boundary surfaces where the pressure will act.
6) Repeat steps 2)–5) until the constraint volume V^* is achieved and the convergence criterion (23) is satisfied.

It is noted that the initial structure without any loads will make all the sensitivity numbers equal to zero and thus the iteration will not proceed from the very start. The simple trick to solve this problem is to generate one void element randomly. It has

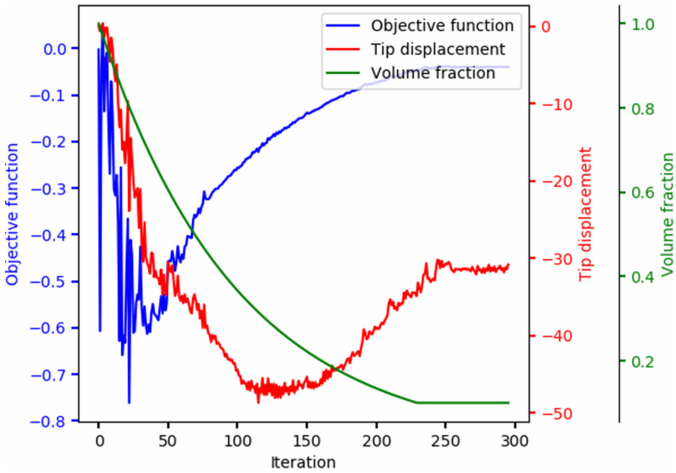

Fig. 3. Evolutionary history of the objective function, tip displacement, and volume fraction when BESO starts from the full design.

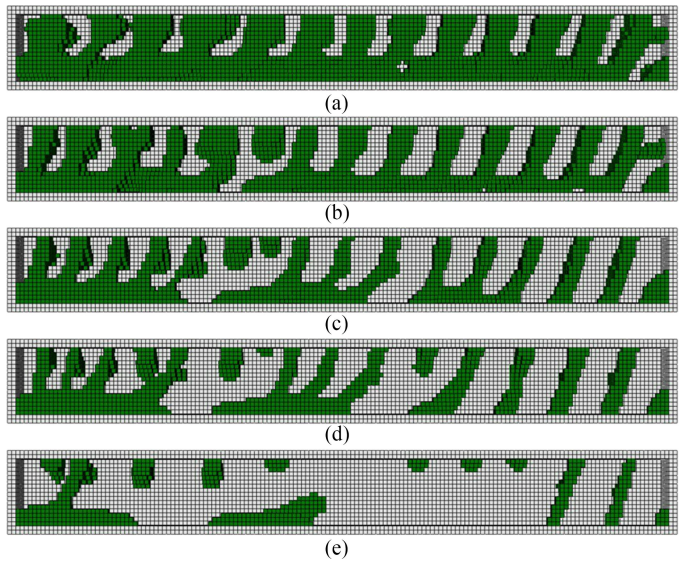

Fig. 4. Evolutionary history of topology. (a) Iteration 40. (b) Iteration 80. (c) Iteration 115. (d) Iteration 160. (e) Final solution (iteration 295).

been tested that the choice of the initial void element has minor effect on the final result because the objective function and tip displacement of the final convergent solutions are very close.

As an aside, the load surfaces can be easily identified and searched out using ABAQUS scripting function since hard-kill BESO method is adopted. We can easily get an array of elements adjacent to the void elements. Then the mesh face shared by the two adjacent elements can be found out and the pressure will act upon these boundary faces.

In terms of computational time, thanks to the powerful parallel computation capability of ABAQUS, it takes about 1 min averagely for each iteration with eight processors and one GPGPU for acceleration.

B. Optimized Results

The geometry parameters for the SPBA designs illustrated in Section II-A are $L = 160$ mm, $W = 20$ mm, and $t = 2$ mm. It means that the design domain is 156 mm in length, 16 mm in height, and 8 mm in width. The whole domain is meshed using $1 \times 1 \times 1$ eight-node structured linear brick elements. Young's modulus of 1 MPa and the air pressure p_0 of 0.05 MPa are assumed. The prescribed constraint volume fraction V^* is usually set to 50%. The BESO parameters used in this example are as follows: $ER = 1\%$, $AR_{\max} = 5\%$, $r_{\min} = 4$ mm, and $\tau = 0.01\%$. The choice of the volume constraint V^* is usually based on the actual design requirement. For example, if a lightweight actuator is required, then choose a low value of V^*. Also, for those who only care about the maximum deformation, we offer a two-step method to fulfil this task, which is as follows.

1) Choose a fairly low value 10% of V^*, and then run the BESO method illustrated above.
2) Find out the iteration where the tip displacement reaches minimum, change the value of V^* to the volume fraction of this iteration, and then rerun the BESO method from this iteration.

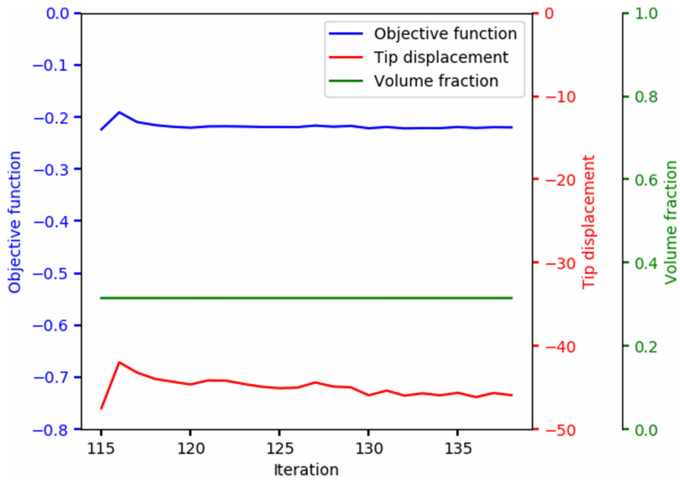

Fig. 5. Evolutionary history of the objective function, tip displacement, and volume fraction when BESO reruns from iteration 115.

For the first step where V^* is set to 10%, Fig. 3 shows the evolutionary history of the objective function h, tip displacement u_{out}, and the volume fraction V_k. The objective function converges to a stable value at the final stage. Fig. 4 shows the evolutionary history of the topology. However, an optimal design with the volume fraction of 10% is not what we expect, because the tip displacement is too small. We hope that the tip displacement falls in the vicinity of the minimum value, so it is what the second step does.

For the second step, we found that the tip displacement reached the minimum value of -48.7 mm at iteration 115, where the volume fraction is 31.5%. Fig. 5 shows the evolutionary history when BESO reruns from iteration 115 after V^* is set to 31.5%. Fig. 6 shows the final convergent optimized topology. As can be seen from Figs. 4(c) and6, even if the difference of

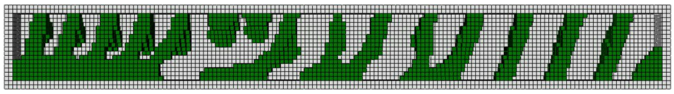

Fig. 6. Final convergent optimized topology at iteration 138.

the objective function is small, the corresponding topologies could be quite different. However, a convergent design with its objective function slightly worse than that of the minimum would be obtained as an optimal solution.

It should be pointed out that general static steps of FEA simulation are adopted in ABAQUS without considering geometrical and material nonlinearity. In fact, the nonlinear analysis is not necessary for the BESO method. First, as mentioned previously, the hard-kill BESO method is a natural way to solve the problem that large displacements of the void elements may change the element stiffness matrix [23]. Second, there is no need to predict exceedingly accurate behaviors of SPBAs in the topology optimization problems. Last but not least, nonlinear analysis requires a much larger amount of computational time than that of linear analysis and may even lead to convergence difficulty problem. From the viewpoint of the application prospects, developers are still required to fine-tune the mesh by filtering out the trivial solid or void elements that are useless in mechanics [26].

IV. Fabrication and Testing

To validate the performance of the optimal design of SPBA created by the BESO method, we fabricate an SPBA prototype based on the optimal topology shown in Fig. 6 and test it in terms of evaluations of its free travel. Free travel measuring experiments is conducted to evaluate the bending deformation. Moreover, the mechanical behavior of SPBA's free travel is simulated under nonlinear FEA, from which we can infer whether our method can really produce a feasible and optimal solution.

A. Material and Fabrication

Instead of the molding and casting method for the traditional SPBAs, we fabricate our SPBAs through 3-D printing technique due to its simple and fast process. The SPBAs are required to achieve large bending deformation and sustain large strain, therefore the selected 3-D printing material must be flexible enough with high rupture strain. Herein, a superior rubber-like photopolymer, Agilus30 Black, is adopted as the soft material for 3-D printing. With a Shore A value of 30 in black, Agilus30 Black has an elongation of 220–270% at break and a tensile strength of 2.4–3.1 MPa. This material is used to get durable and tear-resistant prototypes that can stand up to repeated bending.

The 3-D printing technology is PolyJet, which makes complex shapes, intricate details, and smooth surfaces possible due to its fine resolution. Since complex geometries of SPBAs are involved, soluble supports are required and have to be removed in the postprocess. It means that we cannot print a closed model directly. Therefore, the SPBA is separated into the following two parts: the main body containing the chambers with the dimension of $160 \times 20 \times 18$, and a bottom layer with the dimension of $160 \times 20 \times 2$. These two parts are printed respectively and then glued together. It is noted that several solid elements of the main body are removed to make the chambers fully connected. Since the mesh size (1 mm) is much bigger than the resolution of the printer, the STL files of the SPBA geometries obtained from the mesh model can be directly imported into the PolyJet printer for fabrication, creating precision prototypes. The whole process takes about 2 h.

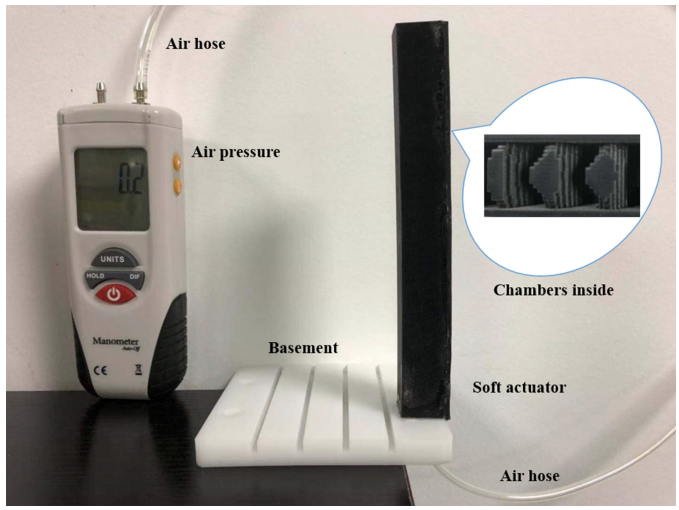

Fig. 7. Experimental setup for the free travel test of the SPBA.

TABLE I
Material Property of Agilus30 Black

C_{10}	C_{01}	C_{20}	C_{11}	C_{02}	D_1	D_2
-0.4889	0.7147	0.07929	-0.2704	0.4709	0.4574	0.0

B. Free Travel Tests

The test setup for the SPBA's free travel is shown in Fig. 7. The fine details have been perfectly printed, validating the feasibility of the proposed method. To eliminate the effect of gravity, the bottom end is clamped on a rigid basement and the top end is free, emulating the same boundary conditions as those of the topology optimization process.

To compare the performance of SPBA between simulations and experiments, the final convergent optimized topology is simulated under nonlinear FEA. In nonlinear FEA, Agilus30 is modeled as an isotropic material and follows a second-order polynomial hyperelastic approximation with coefficients given in Table I [31]. The strain energy function U is defined by

$$U = \sum_{i=0,j=0}^{n} C_{ij}(I_1-3)^i(I_2-3)^j + \sum_{i=1}^{n} \frac{(J-1)^{2i}}{D_i}. \quad (24)$$

In addition, to accurately predict the mechanical behavior of the SPBA, we remesh the SPBA geometries using tetrahedral elements under hybrid control with the approximate global size of 1 mm. It makes the simulated results more reliable.

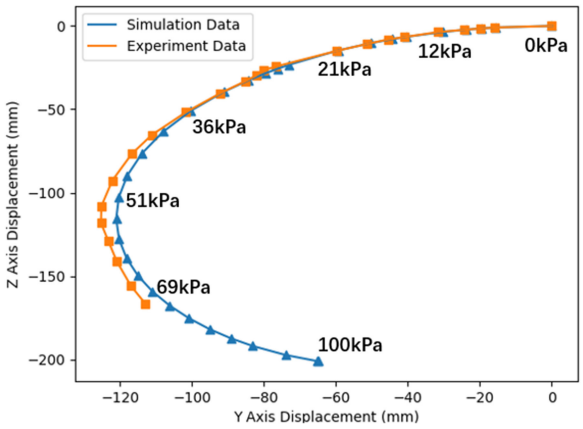

Fig. 8. Comparison of nonlinear FEA bending curvature and experimental data.

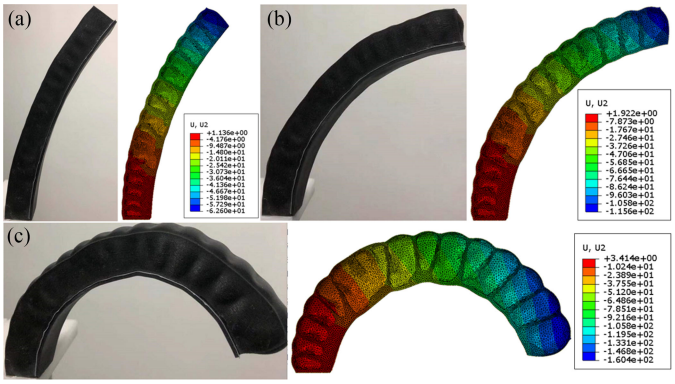

Fig. 9. Comparison of experimental and nonlinear simulated geometries of the optimal SPBA under pressure at: (a) 21 kPa, (b) 36 kPa, and (c) 66 kPa.

To measure the tip displacement, the SPBA was pressurized with air and depressurized three times and meanwhile we use a 3-D camera to capture its bending deformation. The actuation pressure is also recorded meanwhile. After the postprocess of the captured images, the mean experimental results of the tip displacement along the y-axis and z-axis are obtained, as plotted in Fig. 8 together with the simulated results. The maximum absolute error of the tip displacement between the simulations and experiments is 4.72%. It is noted that the experimental results do not include the data where the air pressure exceeds 69 kPa. The reason is that when the actuation pressure is too large, the structure starts to rupture resulting in air leakage. Fig. 9 illustrates the experimental and numerical geometries of the optimal SPBA. The good agreement between the experimental and nonlinear simulated results shows the efficiency of the developed method in designing soft actuators. The verified BESO method can be used to design SPBAs with complex geometries and great bending capability.

V. Extensions and Validation

The BESO method is well structured as mentioned above and establishes a framework for modeling and designing SPBAs.

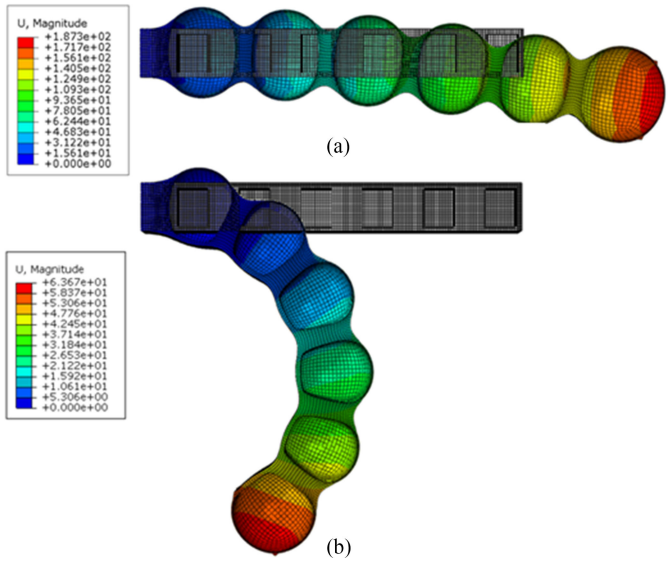

Fig. 10. Comparison of simulated results of the PneuNets under pressure at 0.1 MPa using nonlinear FEA: (a) without strain limiting layer and (b) with strain limiting layer.

Therefore, it can be easily extended to achieve other objectives conditioned on various design requirements with quite limited adjustments to the current process. It is the reusability and extensibility of this method that make it possible to create novel designs of soft actuators without any hypothesis-to-test process.

A. Strain Limiting Layer

Composed of single soft materials, the obtained SPBAs above are expected to undergo large deformation but exert low payloads. If we want the SPBAs to undergo higher pressure and exert higher payloads, we may add some hard materials to the SPBAs. A simple approach is to add a thin unstretchable strain limiting layer [27] in the bottom of the structure like the PneuNets. The strain limiting layer is made of the material that is much more rigid than the one of the soft parts. The merit of PneuNets that they achieve bending motion, to a maximum extent, is due to the strain limiting layer. As a matter of fact, without the strain limiting layer the PneuNets will not bend at all as is evident from Fig. 10. Exactly, the PneuNets actuator shown in Fig. 10(a) is composed of single soft materials, while the one shown in Fig. 10(b) contains a rigid layer at the bottom. The PneuNets actuator example contains six identical chambers inside.

Now that the topologies of SPBAs without strain limiting layer have been obtained, we attempt to add a strain limiting layer to see what the performance and results would be. It is easily achieved by adding four-node linear membrane elements covering the bottom of the structure completely, which represent a thin shell. The rigid material, of which Young's modulus is 5 GPa, is assigned to the rigid elements in this paper. Apart from this procedure, the BESO method is directly applied with no other changes since only the off-design domain is altered and the design domain is not. The volume constraint V^* is set to

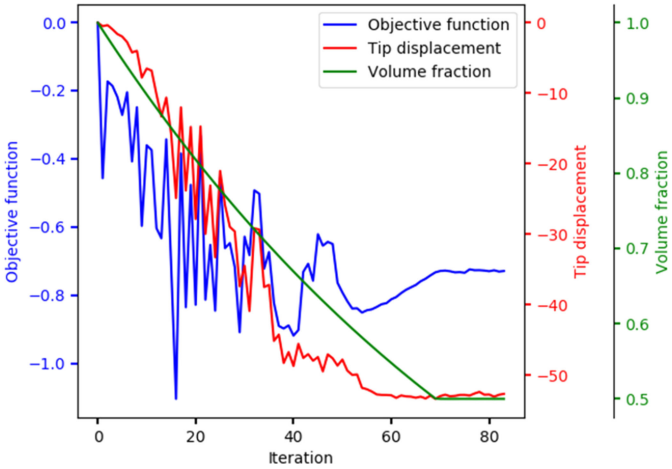

Fig. 11. Evolutionary history of objective function, tip displacement, and volume fraction for the SPBA with strain limiting layer.

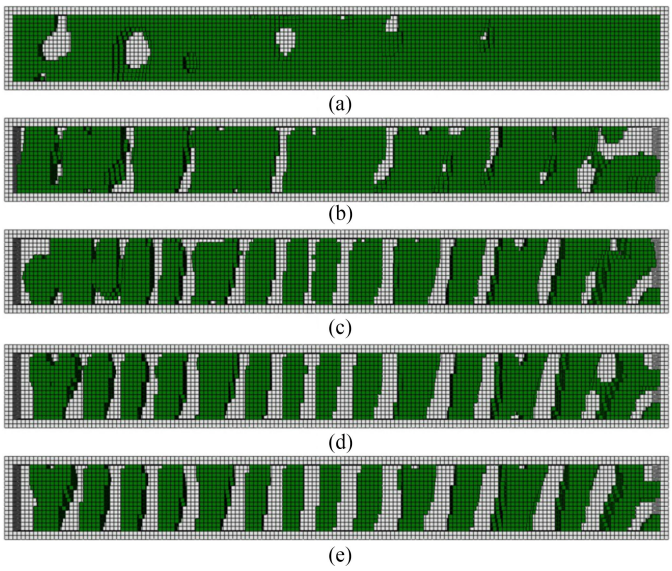

Fig. 12. Evolutionary history of topology with strain limiting layer. (a) Iteration 15. (b) Iteration 30. (c) Iteration 45. (d) Iteration 60. (e) Final solution (iteration 83).

50%, which is equal to the volume fraction in Fig. 10. Other parameters are the same as those mentioned in Section III-B.

Fig. 11 shows the evolutionary history of the objective function, tip displacement, and the volume fraction after adding a strain limiting layer. Fig. 12 shows the evolutionary history of the topology after adding a strain limiting layer. As expected, the final optimized topology shown in Fig. 12(e) is very close to the PneuNets. It reflects the strong practicality and validity of the BESO method of designing SPBAs. The main difference is that the sides of the chambers in the optimized topology have stepped distribution characteristics. The number of chambers is 15 totally in the final optimized topology.

The final optimized result is simulated to compare its performance characteristics to the PneuNets [see Fig. 10(b)]. Note that hexahedral mesh is used in this section for high speed

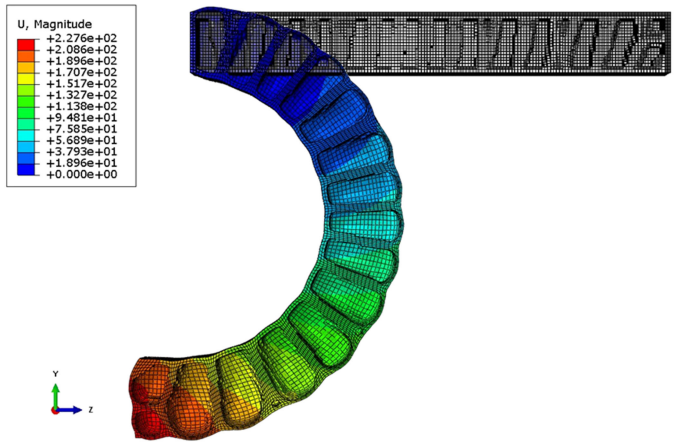

Fig. 13. Simulated results of the final optimized topology with strain limiting layer under pressure at 0.1 MPa using nonlinear FEA.

computation. The bending degree of the optimal topology shown in Fig. 13 is higher than that of the PneuNets shown in Fig. 10(b). Moreover, in the case of the same volume fraction, the mean compliance, i.e., the strain energy of the optimized topology is 1647 N·mm, while the mean compliance of the PneuNets is 2591 N·mm under nonlinear FEA. It means that the optimized SPBAs are stiffer than the PneuNets example, which may make the optimized topology more reliable. Therefore, the optimized SPBAs are able to undergo higher pressure resulting in more deformations or higher resistant force. Moreover, through our method, we can determine the shape, size, and number of the chambers of the SPBAs directly. Generally, our method is faster and better to design SPBAs compared to the enumeration method to design PneuNets [11].

B. Initial Guess Design

The two-step method for selecting V^* shows that the BESO method can find the optimal topology by starting from any intermediate iteration. Before the constraint volume is reached, the BESO method is actually searching for an appropriate guess design for later iterations. Therefore, we can use the BESO method directly by starting from an initial guess design, which has a volume close to the objective volume. It means that in our framework, the initial design inspired by biomimetics can be optimized to achieve maximum design requirements. Another advantage of starting from the guess design is that the number of iterations can be markedly decreased.

Let us assume that the topology optimization of SPBA is started from the initial guess design shown in Fig. 14(a) with a strain limiting layer in the bottom, the same as the PneuNets shown in Fig. 10. To validate the optimality, the constraint volume V^* is equal to the volume fraction of the guess design, i.e., 50%. The final topology is shown in Fig. 14(b). Fig. 15 shows the evolution history of the objective function and the tip displacement. It indicates that the present method can lead to a convergent solution even from an initial guess design. The convergent vertical tip displacement 53 mm is quite larger than that of the initial topology 23 mm. Figs. 16 and 13 show that both

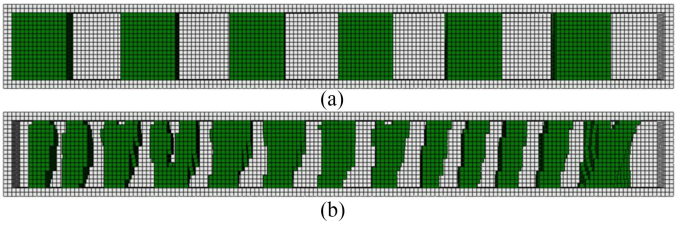

Fig. 14. SPBA topology optimization starts from an initial guess design. (a) Initial guess design. (b) Final topology.

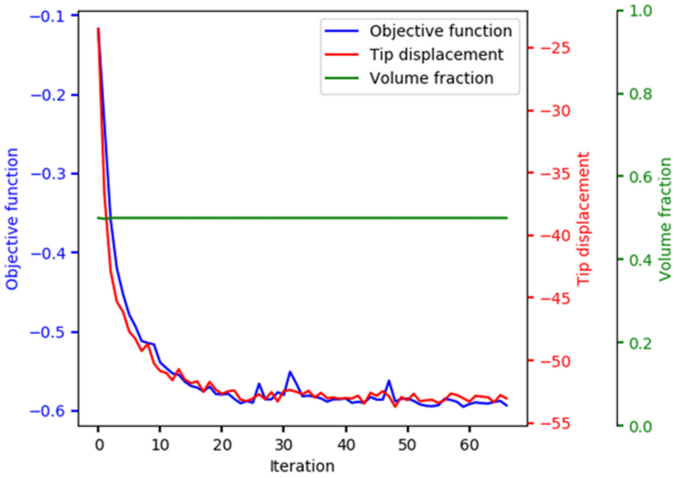

Fig. 15. Evolutionary history of objective function and tip displacement when starting from an initial guess design.

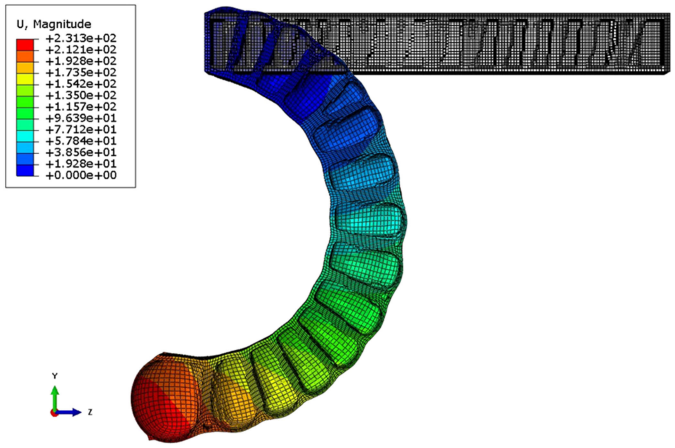

Fig. 16. Simulated results of the final optimized topology when starting from an initial guess design under pressure at 0.1 MPa using nonlinear FEA.

the two optimal designs have similar bending capability. The mean compliance of the optimized topology shown in Fig. 16 is 1772 N · mm.

The optimal design starting from an initial guess design or full design can lead to a convergent solution. Now we can compare the optimal design shown in Fig. 12(e) starting from full design with that shown in Fig. 14(b) starting from guess design. The tip

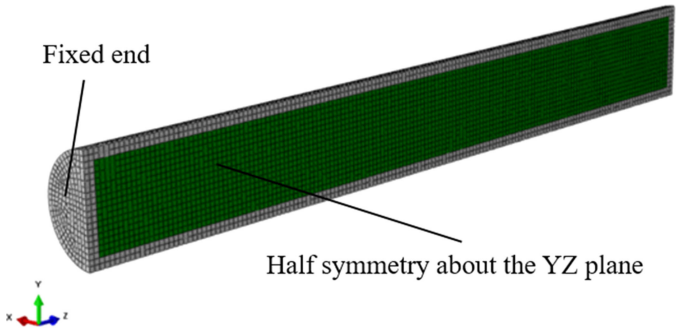

Fig. 17. Prototype of a circular cylindrical SPBA. Note that it is modeled in half-symmetry.

displacements are very close, but the objective functions and the mean compliances are a bit different. The one starting from a full design has a lower mean compliance and objective function, thus it is a better design. This example demonstrates that the BESO method can help to optimize the bionic design of SPBA. However, starting from an initial guess design may sometimes converge to a local optimum because some void elements in the initial guess design may never be included in the FEA during the whole optimization process.

C. Geometric Shape

The specific geometric shape of the SPBAs can be instantly considered by the proposed BESO implementation. In the graphical interface of ABAQUS, arbitrarily shaped geometries, usually rod-based SPBAs [28], can be created and then taken as the design domain after meshing. The previous BESO implementations are based on regular design domain of three-dimensional rectangular solids, which are meshed with structured brick elements, i.e., cuboid elements.

Nevertheless, other kinds of rods will result in a fine mesh of unstructured brick elements. Here we take a circular cylindrical SPBA as an example (see Fig. 17). The radius is 10 mm and length is 160 mm with the wall thickness of 2 mm similar to the rectangular solid SPBAs. It can be seen that the circular cylinder has to be meshed with unstructured elements. The approximate mesh size is 1 mm.

When an unstructured mesh is assigned, the sensitivity number should consider the effect of the volume of each element V_e. From (17), the sensitivity number of the *eth* element becomes

$$\alpha_e = \begin{cases} \dfrac{1}{V_e}\left(C\boldsymbol{\lambda}_e^{\boldsymbol{T}}\boldsymbol{K}_e^0\boldsymbol{u}_e - \dfrac{1}{2}u_{\text{out}}\boldsymbol{u}_e^{\boldsymbol{T}}\boldsymbol{K}_e^{\boldsymbol{0}}\boldsymbol{u}_e\right) & (x_e = 1) \\ 0 & (x_e = 0) \end{cases}. \tag{25}$$

Actually the load change in the *eth* element $\partial \boldsymbol{L}_{\boldsymbol{p}}/\partial x_e$ also alters and is no longer a constant vector. It can be easily calculated by distributing the force of each surface to the nodes associated with it. However, it has no effect on the sensitivity number so we decide to let it drop.

Fig. 18 shows the final optimized topology of the circular cylindrical SPBA without and with strain limiting layer. Note

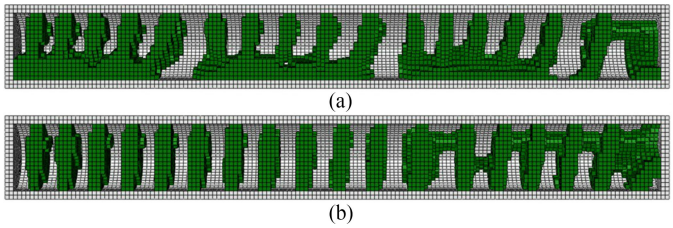

Fig. 18. Final optimized topology of the circular cylindrical SPBAs: (a) without strain limiting layer and (b) with strain limiting layer.

that here the strain limiting layer is attached at the bottom of the circular cylinder that covers one-eighth of its side surfaces. The total number of iteration are 197 and 96, respectively.

D. Objective Function

The objective function can also be changed to satisfy some special requirements. Through the objective function, we can adjust the bending direction of the SPBAs. A simple representation is that if we choose the negative objective function in Section II-B, the SPBA will go upward along the positive y-axis. Another instructive example is given as follows.

We take one kind of soft actuators for thumb rehabilitation as a practical example. The overall motion path of the thumb during opposition grasp can be represented as a combination of rotation about the x-axis and y-axis and extension along the z-axis [29]. It means that we have to create asymmetric SPBAs to solve this problem. The soft fiber-reinforced actuators have been designed for thumb rehabilitation [29], [30]. However, the study on asymmetric SPBAs for thumb rehabilitation is still a blank field.

Thankfully, this problem can be easily solved by changing the objective function. The SPBAs have to rotate about both the x-axis and y-axis. Similar to the precedent mentioned in Section III-B, the SPBA is initialized as a $20 \times 20 \times 160$ rectangular solid with the wall thickness of 2. It should be noted that in this example the SPBA is not modeled in half-symmetry. Then from (1), the objective function becomes

$$\begin{aligned} &\text{Minimize}: h(x_1,\ x_2,\ \ldots,\ x_N) = \frac{u_x+u_y}{C} \\ &\text{With}: \quad u_x + u_y = \boldsymbol{L^*_{\mathbf{out}}}^{\boldsymbol{T}}\boldsymbol{U} \end{aligned} \tag{26}$$

where u_x and u_y are the tip displacement along the x-axis and y-axis, respectively. $\boldsymbol{L^*_{\mathbf{out}}}$ is a vector full of 0s except for a 1 at the output node corresponding to the displacement along the x-axis and y-axis. As the virtual load vector is changed, multiple load cases should be considered. It can be conveniently achieved by adding a concentrated force along the x-axis at the tip of the SPBA in ABAQUS. The volume constraint V^* is set to 50%.

The total number of iteration is 172. Although it is difficult to display the inner structure in the whole SPBA, we show the simulated results of the final optimized topology using nonlinear FEA (see Fig. 19). It is seen that the special SPBA achieves the flexible bending motion about the x-axis and the y-axis as the thumb does during opposition grasp.

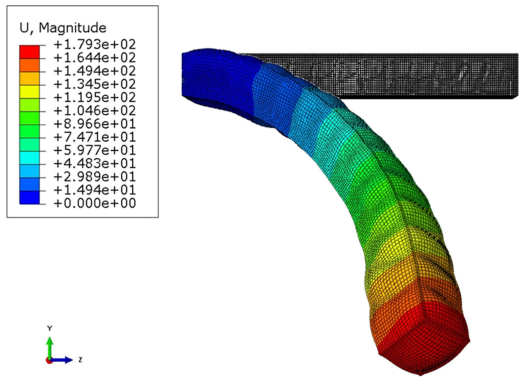

Fig. 19. Simulated results of the final optimized topology of the asymmetric SPBA for thumb rehabilitation under pressure at 0.1 MPa using nonlinear FEA.

VI. Conclusion

We have presented a numerical topology optimization method and its validated simulation and experimental results for the optimal design of SPBAs subjected to design-dependent pressure loads. This method can aid researchers in overcoming current challenges on automatic SPBA designs conditioned on customized design requirements. Exactly, our study makes it efficient and economical to design SPBAs and enables researchers to explore the universe of solutions created by the combination of the structure and design requirements. To show the validity and utility of the proposed approach, rectangular solid and circular cylindrical SPBAs with and without strain limiting layer are designed, which achieve their maximum bending motion. Furthermore, the asymmetric SPBA for thumb rehabilitation is created by changing the objective function. The proposed systematic method can be applied extensively to create more novel designs of SPBAs.

Additionally, this paper is the first attempt at the mathematical formula to design soft actuators subjected to design-dependent pressure loads. It explains the scientific nature and rational structure of the existing PneuNets actuators. More importantly, the topology optimization method provides theoretical guidance for engineering practical purposes of manufacturing soft actuators. Further work will apply this framework to create novel soft actuators by taking more constraints into account, or extend the capabilities of the method to enhance its accuracy.

References

[1] C. Lee *et al.*, "Soft robot review," *Int. J. Control Autom. Syst.*, vol. 15, no. 1, pp. 3–15, 2017.
[2] D. Rus and M. T. Tolley, "Design, fabrication and control of soft robots," *Nature*, vol. 521, no. 7553, pp. 467–475, 2015.
[3] D. Popov, I. Gaponov, and J. H. Ryu, "Portable exoskeleton glove with soft structure for hand assistance in activities of daily living," *IEEE/ASME Trans. Mechatronics*, vol. 22, no. 2, pp. 865–875, Apr. 2017.
[4] J. Hughes *et al.*, "Soft manipulators and grippers: A review," *Frontiers Robot. AI*, vol. 3, pp. 1–12, 2016.
[5] C. Majidi "Soft robotics: A perspective—Current trends and prospects for the future," *Soft Robot.*, vol. 1, no. 1, pp. 5–11, 2014.

[6] C. Xiang, J. Guo, Y. Chen, L. Hao, and S. Davis, "Development of a SMA-fishing-line-McKibben bending actuator," *IEEE Access*, vol. 6, pp. 27183–27189, 2018.
[7] D. A. Marchese, C. D. Onal, and D. Rus, "Autonomous soft robotic fish capable of escape maneuvers using fluidic elastomer actuators," *Soft Robot.*, vol. 1, no. 1, pp. 75–87, 2014.
[8] S. Seok, C. D. Onal, K. Cho, R. J. Wood, D. Rus, and S. Kim, "Meshworm: A peristaltic soft robot with antagonistic nickel titanium coil actuators," *IEEE/ASME Trans. Mechatronics*, vol. 18, no. 5, pp. 1485–1497, Oct. 2013.
[9] C. Laschi, M. Cianchetti, B. Mazzolai, L. Margheri, M. Follador, and P. Dario, "Soft robot arm inspired by the octopus," *Adv. Robot.*, vol. 26, no. 7, pp. 709–727, 2012.
[10] M. Manti, T. Hassan, G. Passetti, N. D'Elia, C. Laschi, and M. Cianchetti, "A bioinspired soft robotic gripper for adaptable and effective grasping," *Soft Robot.*, vol. 2, no. 3, pp. 107–116, 2015.
[11] P. Moseley, J. M. Florez, H. A. Sonar, G. Agarwal, W. Curtin, and J. Paik, "Modeling, design, and development of soft pneumatic actuators with finite element method," *Adv. Eng. Mater.*, vol. 18, no. 6, pp. 978–988, 2016.
[12] P. Polygerinos *et al.*, "Modeling of soft fiber-reinforced bending actuators," *IEEE Trans. Robot.*, vol. 31, no. 3, pp. 778–789, Jun. 2015.
[13] O. Sigmund. "On the design of compliant mechanisms using topology optimization∗," *J. Struct. Mech.*, vol. 25, no. 4, pp. 493–524, 1997.
[14] J. Hiller and H. Lipson, "Automatic design and manufacture of soft robots," *IEEE Trans. Robot.*, vol. 28, no. 2, pp. 457–466, Apr. 2012.
[15] H. Zhang, A. S. Kumar, F. Chen, J. Y. H. Fuh, and M. Y. Wang, "Topology optimized multimaterial soft fingers for applications on grippers, rehabilitation and artificial hands," *IEEE/ASME Trans. Mechatronics*, vol. 24, no. 1, pp. 120–131, Feb. 2019.
[16] F. Chen *et al.*, "Topology optimized design, fabrication, and characterization of a soft Cable-Driven gripper," *IEEE Robot. Autom. Lett.*, vol. 3, no. 3, pp. 2463–2470, Jul. 2018.
[17] B. Bourdin and A. Chambolle, Design-dependent loads in topology optimization," *Esaim, Control Optim. Calculus Variations*, vol. 9, no. 9, pp. 19–48, 2010.
[18] X. Huang and Y. M. Xie, *Evolutionary Topology Optimization of Continuum Structures: Methods and Applications*. Hoboken, NJ, USA: Wiley, 2010.
[19] Z. H. Zuo and Y. M. Xie, "A simple and compact Python code for complex 3D topology optimization," *Adv. Eng. Softw.*, vol. 85, no. C, pp. 1–11, 2015.
[20] Y. LI, "Topology optimization of compliant mechanics based on the BESO method," Ph.D. dissertation, School Civil, Environ. Chem. Eng., RMIT Univ., Melbourne, VIC, Australia, 2014.
[21] M. Stolpe and K. Svanberg, "An alternative interpolation scheme for minimum compliance topology optimization," *Struct. Multidisciplinary Optim.*, vol. 22, no. 2, pp. 116–124, 2001.
[22] M. Bruyneel and P. Duysinx, "Note on topology optimization of continuum structures including self-weight," *Struct. Multidisciplinary Optim.*, vol. 29, no. 4, pp. 245–256, 2005.
[23] T. E. Bruns and D. A. Tortorelli, "An element removal and reintroduction strategy for the topology optimization of structures and compliant mechanisms," *Int. J. Numer. Methods Eng.*, vol. 57, no. 10, pp. 1413–1430, 2003.
[24] R. Picelli, W. M. Vicente, and R. Pavanello, "Bi-directional evolutionary structural optimization for design-dependent fluid pressure loading problems," *Eng. Optim.*, vol. 47, no. 10, pp. 1324–1342, 2015.
[25] Y. X. Yang, Y. M. Xie, and G. P. Steven, "Evolutionary methods for topology optimisation of continuous structures with design dependent loads," *Comput. Struct.*, vol. 83, no. 12/13, pp. 956–963, 2005.
[26] M. H. Hsu and Y. L. Hsu, "Interpreting three-dimensional structural topology optimization results," *Comput. Struct.*, vol. 83, no. 4/5, pp. 327–337, 2005.
[27] F. Ilievski, A. D. Mazzeo, R. F. Shepherd, X. Chen, and G. M. Whitesides, "Soft robotics for chemists," *Angew. Chemie*, vol. 123, no. 8, pp. 1930–1935, 2011.
[28] K. M. D Payrebrune and O. M. O'Reilly, "On the development of rod-based models for pneumatically actuated soft robot arms: A five-parameter constitutive relation," *Int. J. Solids Struct.*, vol. 120, pp. 226–235, 2017.
[29] P. Maeder-York *et al.*, "Biologically inspired soft robot for thumb rehabilitation," *J. Med. Devices*, vol. 8, no. 2, pp. 1815–1847, 2016.
[30] P. Polygerinos, Z. Wang, K. C. Galloway, R. J. Wood, and C. J. Walsh, "Soft robotic glove for combined assistance and at-home rehabilitation," *Robot. Auton. Syst.*, vol. 73, no. C, pp. 135–143, 2015.
[31] C. du Pasquier, T. Chen, S. Tibbits, and K. Shea, "Design and computational modeling of a 3D printed pneumatic toolkit for soft robotics," *Soft Robot.*, 2019. [Online]. Available: https://www.liebertpub.com/doi/full/10.1089/soro.2018.0095

Yongyu Chen received the B.S. degree in 2017 in the Department of Automation, Shanghai Jiao Tong University, Shanghai, China, where he is currently working toward the MA.Sc. degree under the guidance of Prof. Qunfei Zhao and Zeyang Xia.

His research interests include soft robotics, robotic manipulators, and structural design.

Zeyang Xia (SM'16) received the B.S. degree in mechanical engineering from Shanghai Jiao Tong University, Shanghai, China, in 2002, and the Ph.D. degree in mechanical engineering from Tsinghua University, Beijing, China, in 2008.

He is currently a Full Professor with the Shenzhen Institutes of Advanced Technology, Chinese Academy of Sciences, Shenzhen, China, where he is also the Director of the Medical Robotics and Biomechanics Laboratory. He was or is the PI of over ten research grants, including the National Key Research and Development Project and three National Natural Science Funds. He has authored or coauthored more than 90 peer reviewed papers, and applied for more than 40 patents. His research interests include medical robotics, soft robotics, humanoid robotics, and biomechanics.

Dr. Xia was the recipient of Guangdong Natural Science Funds for Distinguished Young Scholar in 2015, the Wu Wenjun Artificial Intelligence Science and Technology Award (Natural Science) in 2017, and the Xiong Youlun Excellent Young Scholars Award in 2019, respectively. He was the General Chair of IEEE RCAR 2019 and a key organizing member of several other IEEE research conferences. He is the Chairman of the Guangzhou Branch of the Youth Innovation Promotion Association, Chinese Academy of Sciences, and the Co-Chair of the Guangdong Chapter of the IEEE Robotics and Automation Society.

Qunfei Zhao received the B.S.E.E. degree in automation from Xi'an Jiao Tong University, Xi'an, China, in 1982, and the Sc.D. degree in system science from the Tokyo Institute of Technology, Tokyo, Japan, in 1988.

He is currently a Full Professor with the School of Electronic Information and Electric Engineering, Shanghai Jiao Tong University, Shanghai, China. His research interests include robotics, machine vision, and optimal control of complex mechatronic systems.